Distinct surface response to black carbon aerosols

Tao Tang¹, Drew Shindell², Yuqiang Zhang², Apostolos Voulgarakis^{3,4}, Jean-Francois Lamarque⁵, Gunnar Myhre⁶, Gregory Faluvegi^{7,8}, Bjørn H. Samset⁶, Timothy Andrews⁹, Dirk Olivié¹⁰, Toshihiko Takemura¹¹, Xuhui Lee¹

5

⁵National Center for Atmospheric Research, Boulder, CO, USA

⁶CICERO, Center for International Climate and Environment Research, Oslo, Norway

⁷Center for Climate System Research, Columbia University, New York, NY, USA

⁸NASA Goddard Institute for Space Studies, New York, NY, USA

⁹Met Office Hadley Centre, Exeter, UK

15 ¹⁰Norwegian Meteorological Institute, Oslo, Norway

¹¹Kyushu University, Fukuoka, Japan

Correspondence to: Tao Tang (tao.tang@yale.edu)

20

¹School of the Environment, Yale University, New Haven, CT, USA

²Division of Earth and Climate Sciences, Duke University, Durham, NC, USA

³Leverhulmn Centre for Wildfires, Environment and Society, Department of Physics, Imperial College London, London, UK ⁴School of Environmental Engineering, Technical University of Crete, Chania, Greece.

Abstract. For the radiative impact of individual climate forcings, most previous studies focused on the global mean values at the top of the atmosphere (TOA) and less attention has been paid to surface processes, especially for black carbon aerosols. In this study, the surface radiative responses to five different forcing agents were analyzed by using idealized model simulations. Our analyses reveal that for greenhouse gases, solar irradiance and scattering aerosols, the surface temperature changes are mainly dictated by the changes of surface radiative heating, but for BC, surface energy redistribution between different components plays a more crucial role. Globally, when a unit BC forcing is imposed at TOA, the net shortwave radiation at the surface decreases by -5.87±0.67 W m⁻² per W m⁻² (averaged over global land without Antarctica), which is partially offset by increased downward longwave radiation (2.32±0.38 W m⁻² per W m⁻²) from the warmer atmosphere, causing a net decrease in the incoming downward surface radiation of -3.56±0.60 W m⁻² per W m⁻². Despite a reduction in the downward radiation energy, the surface air temperature still increases by 0.25±0.08 K because of less efficient energy dissipation, manifested by reduced surface sensible (-2.88±0.43 W m⁻² per W m⁻²) and latent heat flux (-1.54±0.27 W m⁻² per W m⁻²), as well as a decrease of Bowen ratio (-0.20±0.07 per W m⁻²). Such reductions of turbulent fluxes can be largely explained by enhanced air stability (0.07±0.02 K per W m⁻²), measured as the difference of the potential temperature between 925 hPa and surface, and reduced surface wind speed (-0.05±0.01 m s⁻¹ per W m⁻²). The enhanced stability is due to the faster atmospheric warming relative to the surface whereas the reduced wind speed can be partially explained by enhanced stability and reduced equator-to-pole atmospheric temperature gradient. These rapid adjustments under BC forcing occur in the lower atmosphere and propagate downward to influence exerted a 'top down' impact on the surface energy redistribution and thus, surface temperature response, which is not observed under greenhouse gases or scattering aerosols. Our study provides new insights into the impact of absorbing aerosols on surface energy balance and surface temperature response.

1 Introduction

60

Black carbon (BC) aerosols, emitted from diesel engines, biofuels, forest fires, incomplete combustion and biomass burning, could significantly impact the Earth's climate by changing its radiative balance or by perturbing the hydrological cycle (Ramanathan et al., 2001; Menon et al., 2002). The former is realized via absorbing solar radiation, causing positive effective radiative forcing (ERF) at the top of the atmosphere (TOA) and thus, warming the climate (Ramanathan & Carmichael, 2008; Bond et al., 2013; Myhre et al., 2013b) while the latter is partly through modifying the microphysical properties of clouds (e.g., albedo and lifetime) (Koch & Del Genio, 2010; Bond et al., 2013; Boucher et al., 2013), which could further impact ERF. For instance, Menon et al. (2002) attributed the cooling and drying trends in North China in the second half of 20th century to BC aerosols; Meehl et al. (2008) suggested that BC contributed to the precipitation change in India by altering the meridional temperature gradient.

For radiative impacts, however, most previous studies have only focused on TOA forcing. TOA forcing is useful in understanding the climate feedback, climate sensitivity, and future climate change (Andrews et al., 2012), but it is not

necessarily predictive of the spatial pattern of surface temperature response, which is more related to surface radiative changes (Wild et al., 2004). One intriguing phenomenon for BC is that, on the global scale, BC could warm the surface even with reduced solar radiation and net radiation at the surface (Ramanathan & Carmichael, 2008), which is somewhat counterintuitive as higher surface temperature generally requires more incoming radiation at the surface. FAQ 7.2 of Boucher et al. (2013) briefly described the heating process induced by BC. Specifically, BC particles firstly heat the atmosphere and cause surface cooling locally, but then warm both the surface and the atmosphere due to atmospheric circulation and mixing processes. When it comes to surface response, Ramanathan et al. (2001) suggested that the reduced solar radiation at the surface is possibly counteracted by reduced evaporation, which further perturbs the hydrological cycle. Krishnan and Ramanathan (2002) found that the source regions of haze are subject to cooling due to the absorption of solar radiation whereas regions outside the source can be warming, thus contributing to overall global warming. Liepert et al. (2004) argued that aerosols and clouds could lead to weakened turbulent flux at the surface.

Wilcox et al. (2016) reported a reduction of turbulent flux under BC aerosols at the surface and linked such responses to clouds. Based on model simulations, Myhre et al. (2018) concluded that BC aerosols can change the global hydrological cycle by suppressing sensible heat flux at the surface, and attributed this suppression to the changes of air stability.

The published studies citied above provide informative insights to the surface radiative responses to BC aerosols. To our best knowledge, however, a clear and detailed mechanism of surface radiative response to BC is still lacking from the perspective of the surface energy balance. In this study, we aim to fill this gap and answer the following scientific questions: (i) How does the surface warming under BC aerosols differ from warming due to greenhouse gases and solar forcing; (ii) What are the specific mechanisms that drive such warming responses; and (iii) what are the relative contribution to the surface temperature change from each surface energy budget component.

2 Data and Methods

2.1 Data

75

80

90

This study employs the model output from the Precipitation Driver and Response Model Intercomparison Project (PDRMIP), utilizing simulations examining the climate responses to individual climate drivers (Myhre et al., 2017). The eight models used in this study are CanESM2, GISS-E2R, HadGEM2-ES, HadGEM3, MIROC, CESM-CAM4, CESM-CAM5 and NorESM. The versions of these models are essentially the same as their versions in the 5th Assessment Report of Intergovernmental Panel on Climate Change (IPCC AR5). The configurations and basic settings are listed in Table 1. In these simulations, five separate perturbations were applied to all the models instantly on global scale: a doubling of CO₂ concentration (CO₂×2), a tripling of CH₄ concentration (CH₄×3), a 2% increase in solar irradiance (Solar+2%), a tenfold increase of present-day black carbon concentration/emission (BC×10), and a fivefold increase of present-day SO₄ concentration/emission (SO₄×5). Each perturbation was run in two parallel configurations, a 15-year fixed sea surface temperature (fsst) simulation and a 100-year

coupled simulation. The former is compared with its fsst control simulation to diagnose the ERF and fast responses in each model, whereas the latter is used to examine climate responses. One model (CESM-CAM4) used a slab ocean setup for the coupled simulation whereas the others used a full dynamic ocean. For aerosol perturbations, monthly year 2000 concentrations were derived from the AeroCom Phase II initiative (Myhre et al., 2013a) and multiplied by the stated factors in concentration-driven models. Some models were unable to perform simulations with prescribed concentrations. These models multiplied emissions by these factors instead (Table 1). The aerosol loadings in the NorESM model for the two aerosol perturbations are shown in Fig. 1 for an illustrative purpose; the spatial patterns are similar for other models. In the BC experiment, the concentration is highest in East China (E. China), followed by India, tropical Africa and South America (S. America). In the current study, these four regions are referred to as source regions due to their high emissions while US and Europe are defined as non-source regions due to their relatively low emissions. For the SO₄ experiment, the aerosols are mainly restricted to the Northern Hemisphere (NH), with the highest loading observed in E. China, followed by India and Europe. The eastern US also has moderately high concentrations. More detailed descriptions of PDRMIP and some PDRMIP findings are given in Samset et al. (2016), Myhre et al. (2017) and Tang et al. (2018).

2.2 Methods

100

105

110

In this study, we start from the surface energy balance. We restrict our discussions to land grids only, because this is where most people live and thus, the temperature response over land is more important to the wellbeing of human. The incoming radiative energy (R_{in}) includes:

$$R_{in} = \downarrow SW - \uparrow SW + \downarrow LW \tag{1}$$

In Eqn. (1), ↓SW represents downward shortwave radiation and ↑SW represents reflected SW radiation. ↓LW denotes the downward LW radiation. The law of energy conservation requires that the R_{in} should be balanced by the outgoing energy
 115 (E_{out}):

$$E_{out} = \uparrow LW + H + \lambda E + G \tag{2}$$

In Eqn (2), ↑LW is the outgoing longwave radiation, which is a function of temperature based on the Stefan-Boltzmann law.

H, λE and G denote sensible heat flux, latent heat flux and ground heat flux, respectively. For latent heat flux (λE), λ is the specific latent heat of evaporation and E is the evaporation rate. R_{in} is defined as surface radiative heating, as it is the radiative input provided to the surface to raise the surface temperature (Wild et al., 2004). The surface responds to the imposed energy by redistributing the energy content through each E_{out} component. Since R_{in} is equal to E_{out}, we have:

125
$$\triangle R_{in} = \triangle \uparrow LW + \triangle H + \triangle \lambda E + \triangle G$$
 (3)

The changes of each energy component, denoted by △, are obtained by subtracting the control simulations from the perturbations using the data of years 6-15 in each fsst simulation and years of 71-100 in each coupled simulation. The changes are then normalized by the ERF in the corresponding experiments to obtain the changes per unit global forcing. Negative values for the energy component, denoted by a negative sign, represent decreasing trends. The ERF values for each model are obtained from Tang et al. (2019), which diagnosed as the combination of net SW radiation plus the ↓LW radiation at the TOA in the fsst simulations (Hansen et al., 2002). The multi-model mean (MMM) ERF values are 3.68±0.09 W m⁻² (CO₂×2), 1.15±0.09 W m⁻² (CH₄×3), 4.21±0.05 W m⁻² (Solar+2%), 1.20±0.28 W m⁻² (BC×10), and -3.63±0.71 W m⁻² (SO₄×5) for indicated experiments (mean±1 standard error). The MMM changes are estimated by averaging all the eight models' results. A two-sided student t-test is used to examine whether the MMM results are significantly different from zero. The same process was repeated for all variables analyzed in the current study.

3 Results

130

135

140

155

3.1 Incoming radiation and surface temperature changes under BC forcing

Figure 2a-c show the MMM changes of Rin and its components for the fsst simulations of the BC experiment. The fsst simulations are analyzed because we mainly focus on the rapid adjustments when the forcing is instantly imposed. Rapid adjustments are generally referred to the fast responses that affect the components of the climate system and modify the global energy budget indirectly. Unlike feedbacks, rapid adjustments do not operate through changes in the global mean temperature and most are thought to occur within a few weeks (Boucher et al., 2013). Specifically, when a unit BC forcing is imposed at the TOA, the net surface SW radiation decreases by -5.87±0.67 W m⁻² due to the absorption of solar radiation by BC particles whereas ↓LW radiation shows an increase of 2.32±0.38 W m⁻² (Fig. 2a & b), as a result of the warmer atmosphere. When combined, R_{in} still decreases by -3.56±0.60 W m⁻² on the global scale, with some positive changes only in high-latitude regions (Fig. 2c). However, the surface air temperature increases globally by 0.25±0.08 K despite the decreased R_{in}, except in the source regions where some slight cooling trends occurred (Fig. 2d). It is noted that these results are for land grids only. The pattern of cooling in the source regions and warming elsewhere agrees well with findings reported by Krishnan and Ramanathan (2002). This type of changes persists into near-equilibrium state, where global mean temperature changes and associated feedbacks are included (Fig. 2e-h). Due to the enhanced warming of the atmosphere and probably water vapor buildup, the LW radiation shows a stronger increase (Fig. 2f), making the R_{in} mostly positive and therefore positive temperature change, except for source regions (Fig. 2g & h). An open question is how the temperature increased with a decreasing R_{in} in the rapid adjustment processes. In order to better understand the mechanisms behind this warming phenomenon, we will explore the E_{out} components in the next section.

3.2 Decomposition of outgoing energy

160

170

175

180

185

Figure 3 depicts the MMM changes of R_{in} and all components of E_{out} in the fsst simulations for all five experiments. The spatial patterns of $\triangle R_{in}$ and $\triangle \uparrow LW$ for the BC experiment were quite different (Fig. 3d & i). Another notable feature is the significant reductions of sensible and latent heat flux in the BC experiment (Fig. 3n & s), which is in agreement with previous studies (Wilcox et al., 2016; Myhre et al., 2018; Suzuki & Takemura, 2019).

These changes are obvious when averaged globally (Fig. 4a and Table 2). The R_{in} decreases by $\pm 3.56 \pm 0.60$ W m⁻², and the H and λE decrease by $\pm 2.88 \pm 0.43$ W m⁻² and $\pm 1.54 \pm 0.27$ W m⁻², respectively, making the energy partitioned to $\triangle \uparrow LW$ positive $(0.86 \pm 0.36 \text{ W m}^{-2})$. In other words, although the radiative heating (R_{in}) decreases, convective and evaporative cooling decrease by a larger amount (124% relative to $\triangle R_{in}$) owing to less efficient energy dissipation, thereby warming the surface and leading to a positive $\triangle \uparrow LW$ radiation. The reduction of turbulent fluxes (H and λE) is found for both source regions and non-source regions (Fig. 4b). In the source regions, the reductions of turbulent flux are nearly the same as the reduction of R_{in} , making the temperature response negligible or only slightly negative. In the non-source regions, the reduction of turbulent fluxes exceeds the reduction of R_{in} , making the temperature response positive. Another interesting phenomenon is that the reduction of H is larger than the reduction of λE for the BC experiment, both on the global scale and in the source regions (Fig. 4). The larger reduction of H indicates a decrease of Bowen ratio (β), defined as the ratio of sensible heat flux over latent heat flux. Globally, β decreases by $\pm 0.20\pm 0.07$ in the BC case, and such drop could reach ± 0.03 in the source regions. In comparison, under other forcing agents, the changes of β are much smaller (the global MMM changes within ± 0.10). The larger change of H is somewhat contradicting to the common sense that λE dominates the turbulent flux on global mean scale. This is because on global scale, 85% of λE is from the ocean (Schmitt, 2008). In this study, we only focus on land grids, in which the λE is largely reduced.

Under other forcing agents, the spatial patterns of $\triangle \uparrow LW$ are similar to the patterns of $\triangle R_{in}$. The changes of H and λE are relatively small and sometimes cancel out each other, making little contributions to temperature change compared with BC (Fig. 3 and 4a). Therefore, the temperature change ($\triangle \uparrow LW$) is dominated by the change of radiative heating ($\triangle R_{in}$). It is worth noting that the decrease of λE in the CO₂ experiment is due the physiological effect of vegetation and plantation (Fig. 3p), which is included in the PDRMIP models (Richardson et al., 2018). It is also noted that the stronger responses in the BC scenario (Fig. 3, 4 and Table 2) could be partially related to its larger changes of surface radiative heating ($\triangle R_{in}$) compared with other forcing agents. Taking CO₂ as an example, $\triangle R_{in}$ is 1.26 W m⁻², similar to its TOA forcing (1 W m⁻²), whereas for BC, $\triangle R_{in}$ is roughly three times larger (Table 2). Observations show that the surface forcing BC could be 10 times larger than TOA forcing on regional scales (Magi et al., 2008). The contributions of G are negligible (Fig. 3u-y) and will not be further discussed.

3.3 Attribution of temperature change

In order to quantify the contributions of each component to $\triangle T$, we applied a multi-linear regression model to the MMM values of $\triangle T$ and the energy components in each experiment, as $\triangle T = a \times \triangle R_{in} + b \times \triangle H + c \times \triangle \lambda E$. Here $\triangle R_{in}$ represents the changes of radiative heating and $\triangle H$ and $\triangle \lambda E$ denote changes in the surface energy redistribution and all grid cells were given equal weight. The results are listed in Table 3. A point-wise comparison of original $\triangle T$ and fitted $\triangle T$ is shown in Fig. S1. These regressions reproduce the $\triangle T$ fairly well, since the correlation coefficients between $\triangle T$ and fitted $\triangle T$ are all above 0.73 and most of the data points align along the one-one line. For CO₂, CH₄, Solar and sulphate aerosols, the coefficients of $\triangle R_{in}$ are one order of magnitude larger than the coefficients of the turbulent fluxes, suggesting that $\triangle R_{in}$ dominates the temperature change under these forcing agents. When it comes to BC, however, $\triangle T$ is more sensitive to $\triangle H$, followed by \triangle R_{in} and $\triangle \lambda E$. With the regression coefficients, we estimated the contributions of each energy component to $\triangle T$ (Fig. 5). In line with our previous results, $\triangle T$ was dominated by surface heating ($\triangle R_{in}$) for most forcing agents with very limited role from turbulent fluxes. BC, nonetheless, is an exception. For BC aerosols, $\triangle T$ is influenced by both surface heating and turbulent fluxes, with the cooling from the former being overwhelmed by the warming from the latter (Fig. 5n, s and x). The domain-averaged changes for the BC experiment are listed in Table 4. Globally, $\triangle H$ produces 0.19 K warming and $\triangle \lambda E$ leads to 0.07 K warming. The combined 0.26 K warming is offset by -0.19 K cooling attributed to reduced $\triangle R_{in}$, producing a net warming of 0.07 K. In terms of percentage, $\triangle H$ and $\triangle \lambda E$ contribute 73% and 27% respectively to the total warming. Such patterns are also seen on regional scales. The warming contributions from $\triangle H$ were $\frac{40}{6}$ (US), $\frac{47}{6}$ (Europe), $\frac{76}{6}$ (E. China), 87% (India), 68% (Africa) and 82% (S. America) and the remaining part were contributed by $\triangle \lambda E$.

3.4 Mechanisms underlying the reduction of turbulent fluxes

The above analyses show that for most of the forcing agents, $\triangle R_{in}$ dominates the surface temperature response while for BC, the surface energy redistribution also comes into play in modifying temperature response as a result of the significant reductions of turbulent fluxes. The next question is why turbulent fluxes decrease substantially in response to BC particles. According to the bulk parameterization of turbulent fluxes, the sensible heat flux is expressed as $Q_{SH} = \rho C_p C_H U(T_s - T_a)$ and latent heat flux as $Q_{LH} = \rho L_v C_E U(q_s - q_a)$. In these two equations, ρ is air density, C_p and L_v are air specific heat capacity and latent heat of vaporization, respectively, C_H and C_E are two exchange coefficients, U denotes surface wind speed, and $U_s - U_s - U_$

195

200

205

Figure 6a-e show the MMM changes of lower tropospheric stability (LTS), defined as the potential temperature difference between 925 hPa and the surface. An enhanced stability is observed for the BC experiment; ΔLTS is 0.0½±0.0½ K averaged globally, in contrast to near zero values from other experiments (-0.0½ K to 0.01 K). The ΔLTS for the NH are even larger, with 0.0½±0.0½ K for BC and -0.0½ to 0.0½ K for other forcing agents. The enhanced LTS, which can significantly impact the sensible heat flux (Myhre et al., 2018), arises from the fact that the BC layers warm faster relative to the surface due to BC absorption of solar radiation. The changes of LTS patterns are similar for 850 hPa and 700 hPa (Fig. S2).

Figure 6f-j portray the MMM changes of surface wind speed. BC causes a much larger decrease of wind speed with respect to other forcing agents, $0.05\pm0.01~\text{m s}^{-1}$ globally compared with zero from other forcing agents. The reduction in wind speed explains the weakening in both sensible and latent heat fluxes according to the bulk parameterization.

Figure 6k-o reveal the changes of humidity gradient (q_s-q_a), defined as the specific humidity difference between the surface and 850 hPa. For CH₄, solar and SO₄, the gradient increases globally with values of 0.02 g kg⁻¹ per W m², 0.01 g kg⁻¹ per W m² and 0.01 g kg⁻¹ per W m² respectively, causing an increase of λE (Figure 3 and 4). For CO₂, the gradient shows slightly negative values (-0.002 g kg⁻¹ per W m²), corresponding to reduced λE (Figure 3 and 4). In terms of BC, the humidity gradient increases by 0.06±0.02 g kg⁻¹ per W m², despite the reduced λE. These analyses illustrate that humidity gradient may also influence latent heat flux for CO₂, CH₄, solar and scattering aerosols. For BC, on the other hand, change of wind speed is the primary driver of the reduction of λE and humidity gradient is of less importance.

Now the last question is why the surface wind speed decreases under BC forcing? The first potential explanation is the abovementioned enhanced LTS. Jacobson and Kaufman (2006) has clearly demonstrated that the enhanced LTS and reduced turbulent exchange can reduce the turbulent kinetic energy and vertical transport of horizonal momentum, thereby reducing surface wind speed. The second possible explanation is that from the dynamical perspective, wind speed is controlled by the pressure gradient force (PGF), the Coriolis force, the gravitational force and the frictional force. PGF is the driving force for atmospheric motion and is potentially the main driver for the changes of wind speed in the current idealized experiments. On global scale, the excessive heating in the tropics with respect to middle and high latitudes causes PGF to point toward polar regions. Here we hypothesize that the decrease of temperature gradient between the equator and poles under BC forcing weakened the PGF and slowed down the wind speed. Evidence in support of this hypothesis is found in Figure 7a-e showing the zonal mean atmospheric temperature change. Mechanistically, BC caused a larger atmospheric heating in the middle latitudes of NH (30°N~60°N) relative to tropics due to more of the BC forcing being located at middle latitudes of NH (Fig. 7d). The faster warming of middle latitudes weakened the PGF between the equator and polar regions, as seen from the larger increase of geopotential height of 500 hPa in the middle latitude regions (Fig. 7i). These patterns are not observed in the other experiments. The changes of geopotential height at other levels show similar results (Fig. S3).

To further understand the relationship between changes in wind speed and temperature, we defined a temperature gradient index (Allen et al., 2012) as $2 \times \triangle T_{30-60} - (\triangle T_{0-30} + \triangle T_{60-90})$, where $\triangle T$ is the mass-weighted (300~850 hPa) temperature response, and subscripts 0-30, 30-60 and 60-90 denote low (0°~30°N), middle (30°N~60°N), and high (60°N~90°N) latitudinal zones, respectively. When the index becomes more positive, middle latitudes warm faster, and a stronger reduction of wind speed is expected. The results for each individual model and experiment are shown in Fig. 8. A reasonably good correlation is seen in the BC scenario (r = -0.59): a larger change in the temperature gradient index corresponds to a stronger decrease in wind speed. The results for other experiments are mostly scattered around zero.

On regional and local scales, several other factors might also contribute to surface wind change (Wu et al., 2018). For instance, the aerosols in Asia have been reported to modify the land-sea temperature contrast, and thus modify monsoon circulation (Xu et al., 2006; Meehl et al., 2008). The different phases of internal variability (e.g., ENSO and NAO) could modulate the circulations on interannual to multi-decadal time scales (Jerez et al., 2013; Hu & Fedorov, 2018). Bichet et al. (2012) suggested that changes in the surface roughness length may also change the wind speed. These factors are not considered in the present study.

4 Discussion and Summary

Our analyses demonstrate that under BC forcing, surface energy redistribution plays a vital role in modifying the surface temperature due to the changes in turbulent fluxes. The changes of turbulent fluxes are consequences of a 'top down'downward influence from the atmosphere. The warming BC layers resulting from absorption of solar radiation in the atmosphere enhances air stability and reduces wind speed. As a result, the surface turbulent fluxes are suppressed. This mechanism is not observed for other forcing agents such as greenhouse gases and scattering aerosols. A similar 'top-down' mechanism has been previously observed in the solar forcing, in which the stratosphere ozone reacts to the UV part of the solar variability and produces additional heating, leading to changes of circulation in the stratosphere. The changes in the stratosphere modify tropical tropospheric circulation that may impact the surface climate (Haigh, 1996; Gray et al., 2010). It is noted that the 'top down' mechanism of solar forcing is not included in the current PDRMIP models. The solar experiments in our analyses are restricted to the surface response to increased solar radiation, which is 'bottom up' mechanism.

As noted in section 3.1, our above analyses mainly focus on the rapid adjustments, which are part of ERF by definition (Boucher et al., 2013). For the BC experiment, these adjustments drive the surface to respond to the forcing. Most of the changes seen in the rapid adjustment stage extended into the near-equilibrium (Fig. S4-S5). For BC forcing, $\triangle R_{in}$ in near-equilibrium state is close to zero with large inter-model spread $(0.20\pm1.19~W~m^{-2})$ instead of strong negative values $(3.42\pm0.51~W~m^{-2})$ in the rapid adjustment stage. The near-zero R_{in} in equilibrium is mainly due to larger $\downarrow LW$ radiation and feedbacks. The equilibrium turbulent flux H and λE are lowered by $\pm 2.57\pm0.39~W~m^{-2}$ and $\pm 1.54\pm0.27~W~m^{-2}$ respectively, which are

comparable in magnitude to changes in the rapid adjustment stage. Such reductions of the equilibrium turbulent fluxes are found in both source regions and non-source regions. Since less energy dissipated away from the surface, more energy $(4.34\pm0.74~\mathrm{W~m^{-2}})$ was partitioned into $\triangle LW$, warming the surface by $0.87\pm0.13~\mathrm{K}$. Fig. S6 shows the slow responses under each forcing, which are obtained by subtracting the rapid adjustments from the coupled simulations. The slow responses are driven by global mean temperature change alone. Interestingly, the spatial patterns are quite similar across different forcing agents. It is further confirmed our finding that it is the rapid adjustment that led to the different surface responses to BC.

Two limitations exist in our current study. First, the aerosol-cloud interactions could not be fully represented, because for the models with fixed aerosol concentration, the changes of cloud lifetime do not affect aerosols. Second, for the BC simulations, two models (MIROC and NorESM) include aerosol indirect effects while the remaining ones have only aerosol-radiation interactions included (instantaneous and rapid adjustments). The cloud effects in these two models may slightly modify the SW radiation at the surface (Tang et al., 2020), although the results from these two models do not differ qualitatively from the other models without those effects. We suggest that our conclusions are not sensitive to such cloud effects.

In summary, our study shows that for forcing agents such as GHG, solar and scattering aerosol, $\triangle R_{in}$ dominates the surface temperature response. For BC forcing, the surface energy redistribution also plays an important role. Under BC forcing, the energy is dissipated less efficiently from the surface to the lower atmosphere, which causes warming at the surface despite the reduced radiative heating. The reductions of sensible heat flux accounts for 73% of the surface warming on global scale and $40\sim80\%$ of the warming on regional scales, with the remaining part arising from the reductions of latent heat flux. Such reductions of turbulent fluxes can be explained by enhanced lower tropospheric stability and reduced surface wind speed. The former is attributed to a faster atmospheric warming relative to the surface whereas the latter is associated with enhanced stability and reduced equator-to-pole atmospheric temperature gradient. These analyses contribute to our understanding of the impact of absorbing aerosols on surface radiation and climate.

Data code availability

285

290

305

The PDRMIP model output used in this study are available to public through the Norwegian FEIDE data storage facility. For more information, please see http://cicero.uio.no/en/PDRMIP. The data for generating the figures is study is performed by using Matlab R2019a. The Matlab code is available upon reasonable request.

Competing interests

The authors declare no competing interests.

Author contributions

310

325

330

335

340

T.T. designed this study. T.T. performed data analysis and wrote the initial manuscript. All authors contributed to scientific discussion, results framing and manuscript polishing.

Acknowledgement

We acknowledge the NASA High-End Computing Program through the NASA Center for Climate Simulation at Goddard Space Flight Center for computational resources to run the GISS-E2R model and support from NASA GISS. PDRMIP is partly funded through the Norwegian Research Council project NAPEX (project number 229778). AV is partially funded by the Leverhulme Trust, grant RC-2018-023. Computing resources for CESM1-CAM5 (ark:/85065/d7wd3xhc) simulations were provided by the Climate Simulation Laboratory at NCAR Computational and Information System Laboratory, sponsored by the National Science Foundation and other agencies. X. L. acknowledges support from the US National Science Foundation (grant AGS1933630). T. Takemura is supported by the Japan Society for the Promotion of Science (JSPS) KAKENHI (grant no. JP19H05669), the Environment Research and Technology Development Fund (S-20) of the Environmental Restoration and Conservation Agency, Japan, and the NEC SX supercomputer system of the National Institute for Environmental Studies, Japan. T. Andrews was supported by the Met Office Hadley Centre Climate Programme funded by BEIS and Defra and the Newton Fund through the Met Office Climate Science for Service Partnership Brazil (CSSP Brazil).

References

- Allen, R. J., Sherwood, S. C., Norris, J. R., & Zender, C. S. (2012). Recent northern hemisphere tropical expansion primarily driven by black carbon and tropospheric ozone. *Nature*, 485(7398), 350-354. doi:10.1038/nature11097
- 345 Andrews, T., Gregory, J. M., Webb, M. J., & Taylor, K. E. (2012). Forcing, feedbacks and climate sensitivity in cmip5 coupled atmosphereocean climate models. *Geophysical Research Letters*, 39. doi:10.1029/2012gl051607
 - Arora, V., Scinocca, J., Boer, G., Christian, J., Denman, K., Flato, G., et al. (2011). Carbon emission limits required to satisfy future representative concentration pathways of greenhouse gases. *Geophysical Research Letters*, 38(5). doi:10.1029/2010GL046270
- Bellouin, N., Rae, J., Jones, A., Johnson, C., Haywood, J., & Boucher, O. (2011). Aerosol forcing in the climate model intercomparison project (cmip5) simulations by hadgem2-es and the role of ammonium nitrate. *Journal of Geophysical Research: Atmospheres,* 116(D20). doi:10.1029/2011JD016074
 - Bentsen, M., Bethke, I., Debernard, J., Iversen, T., Kirkevåg, A., Seland, Ø., et al. (2013). The norwegian earth system model, noresm1-m—part 1: Description and basic evaluation of the physical climate. *Geosci. Model Dev*, 6(3), 687-720. doi:10.5194/gmd-6-687-2013
 - Bichet, A., Wild, M., Folini, D., & Schär, C. (2012). Causes for decadal variations of wind speed over land: Sensitivity studies with a global climate model. *Geophysical Research Letters*, 39(11). doi:10.1029/2012GL051685
 - Bond, T. C., Doherty, S. J., Fahey, D. W., Forster, P. M., Berntsen, T., DeAngelo, B. J., et al. (2013). Bounding the role of black carbon in the climate system: A scientific assessment. *Journal of Geophysical Research-Atmospheres*, 118(11), 5380-5552. doi:10.1002/jgrd.50171
- Boucher, O., Randall, D., Artaxo, P., Bretherton, C., Feingold, G., Forster, P., et al. (2013). Clouds and aerosols. In T. F. Stoker, D. Qin, G.
 K. Plattner, M. Tignor, S. K. Allen, J. Boschung, A. Nauels, Y. Xia, V. Bex, & P. M. Midgley (Eds.), Climate change 2013: The

 physical science basis. Contribution of working group i to the fifth assessment report of the intergovernmental panel on climate

 change (pp. 571-657). Cambridge, UK and New York, USA: Cambridge University Press.
 - Collins, W., Bellouin, N., Doutriaux-Boucher, M., Gedney, N., Halloran, P., Hinton, T., et al. (2011). Development and evaluation of an earth-system model—hadgem2. *Geoscientific Model Development*, 4(4), 1051-1075. doi:10.5194/gmd-4-1051-2011
- 365 Gent, P. R., Danabasoglu, G., Donner, L. J., Holland, M. M., Hunke, E. C., Jayne, S. R., et al. (2011). The community climate system model version 4. *Journal of Climate*, 24(19), 4973-4991. doi:10.1175/2011JCLI4083.1
 - Gray, L. J., Beer, J., Geller, M., Haigh, J. D., Lockwood, M., Matthes, K., et al. (2010). Solar influences on climate. *Reviews of Geophysics*, 48(4). doi:10.1029/2009rg000282
 - Haigh, J. D. (1996). The impact of solar variability on climate. Science, 272(5264), 981-984. doi:10.1126/science.272.5264.981
- Hansen, J., Sato, M., Nazarenko, L., Ruedy, R., Lacis, A., Koch, D., et al. (2002). Climate forcings in goddard institute for space studies si2000 simulations. *Journal of Geophysical Research: Atmospheres, 107*(D18). doi:10.1029/2001JD001143
 - Hu, S. N., & Fedorov, A. V. (2018). Cross-equatorial winds control el nino diversity and change. *Nature Climate Change*, 8(9), 798-+. doi:10.1038/s41558-018-0248-0
- Hurrell, J. W., Holland, M. M., Gent, P. R., Ghan, S., Kay, J. E., Kushner, P. J., et al. (2013). The community earth system model: A framework for collaborative research. *Bulletin of the American Meteorological Society, 94*(9), 1339-1360. doi:10.1175/BAMS-D-12-00121.1
 - Iversen, T., Bentsen, M., Bethke, I., Debernard, J., Kirkevåg, A., Seland, Ø., et al. (2013). The norwegian earth system model, noresm1-m-part 2: Climate response and scenario projections. *Geoscientific Model Development*, 6(2), 389. doi:10.5194/gmd-6-389-2013
- Jacobson, M. Z., & Kaufman, Y. J. (2006). Wind reduction by aerosol particles. Geophysical Research Letters, 33(24). doi:10.1029/2006gl027838
 - Jerez, S., Trigo, R. M., Vicente-Serrano, S. M., Pozo-V?zquez, D., Lorente-Plazas, R., Lorenzo-Lacruz, J., et al. (2013). The impact of the north atlantic oscillation on renewable energy resources in southwestern europe. *Journal of Applied Meteorology and Climatology*, 52(10), 2204-2225. doi:10.1175/JAMC-D-12-0257.1
- Kay, J., Deser, C., Phillips, A., Mai, A., Hannay, C., Strand, G., et al. (2015). The community earth system model (cesm) large ensemble project: A community resource for studying climate change in the presence of internal climate variability. *Bulletin of the American Meteorological Society*, *96*(8), 1333-1349. doi:10.1175/BAMS-D-13-00255.1
 - Kirkevåg, A., Iversen, T., Seland, Ø., Hoose, C., Kristjánsson, J., Struthers, H., et al. (2013). Aerosol–climate interactions in the norwegian earth system model–noresm1-m. *Geoscientific Model Development*, 6(1), 207-244. doi:10.5194/gmd-6-207-2013
- Koch, D., & Del Genio, A. D. (2010). Black carbon semi-direct effects on cloud cover: Review and synthesis. *Atmos. Chem. Phys.*, 10(16), 7685-7696. doi:10.5194/acp-10-7685-2010
 - Krishnan, R., & Ramanathan, V. (2002). Evidence of surface cooling from absorbing aerosols. *Geophysical Research Letters*, 29(9). doi:10.1029/2002GL014687
 - Liepert, B. G., Feichter, J., Lohmann, U., & Roeckner, E. (2004). Can aerosols spin down the water cycle in a warmer and moister world? Geophysical Research Letters, 31(6). doi:10.1029/2003GL019060

- 395 Magi, B. I., Fu, Q., Redemann, J., & Schmid, B. (2008). Using aircraft measurements to estimate the magnitude and uncertainty of the shortwave direct radiative forcing of southern african biomass burning aerosol. *Journal of Geophysical Research: Atmospheres,* 113(D5). doi:10.1029/2007JD009258
 - Meehl, G. A., Arblaster, J. M., & Collins, W. D. (2008). Effects of black carbon aerosols on the indian monsoon. *Journal of Climate*, 21(12), 2869-2882. doi:10.1175/2007jcli1777.1
- 400 Menon, S., Hansen, J., Nazarenko, L., & Luo, Y. (2002). Climate effects of black carbon aerosols in china and india. *Science*, 297(5590), 2250-2253. doi:10.1126/science.1075159
 - Myhre, G., Forster, P., Samset, B., Hodnebrog, Ø., Sillmann, J., Aalbergsjø, S., et al. (2017). Pdrmip: A precipitation driver and response model intercomparison project, protocol and preliminary results. *Bulletin of the American Meteorological Society*(2016). doi:10.1175/BAMS-D-16-0019.1
- 405 Myhre, G., Samset, B., Schulz, M., Balkanski, Y., Bauer, S., Berntsen, T., et al. (2013a). Radiative forcing of the direct aerosol effect from aerocom phase ii simulations. *Atmospheric Chemistry and Physics*, 13(4), 1853. doi:10.5194/acp-13-1853-2013
 - Myhre, G., Samset, B. H., Hodnebrog, O., Andrews, T., Boucher, O., Faluvegi, G., et al. (2018). Sensible heat has significantly affected the global hydrological cycle over the historical period. *Nat Commun*, 9(1), 1922. doi:10.1038/s41467-018-04307-4
- Myhre, G., Shindell, D., Bréon, F.-M., Collins, W., Fuglestvedt, J., Huang, J., et al. (2013b). Anthropogenic and natural radiative forcing.

 In Climate change 2013: The physical science basis. Contribution of working group i to the fifth assessment report of the intergovernmental panel on climate change. Cambridge, UK and New York, USA: Cambridge University Press.
 - Neale, R. B., Richter, J. H., Conley, A. J., Park, S., Lauritzen, P. H., Gettelman, A., et al. (2010). Description of the near community atmosphere model (cam 4.0). Retrieved from Boulder, CO, USA: https://www.ccsm.ucar.edu/models/ccsm4.0/cam/docs/description/cam4_desc.pdf
- 415 Otto-Bliesner, B. L., Brady, E. C., Fasullo, J., Jahn, A., Landrum, L., Stevenson, S., et al. (2016). Climate variability and change since 850 ce: An ensemble approach with the community earth system model. *Bulletin of the American Meteorological Society*, 97(5), 735-754. doi:10.1175/BAMS-D-14-00233.1
 - Ramanathan, V., & Carmichael, G. (2008). Global and regional climate changes due to black carbon. *Nature Geoscience*, 1, 221. doi:10.1038/ngeo156
- 420 Ramanathan, V., Crutzen, P. J., Kiehl, J. T., & Rosenfeld, D. (2001). Aerosols, climate, and the hydrological cycle. *Science*, 294(5549), 2119-2124. doi:10.1126/science.1064034
 - Richardson, T. B., Forster, P. M., Andrews, T., Boucher, O., Faluvegi, G., Flaschner, D., et al. (2018). Carbon dioxide physiological forcing dominates projected eastern amazonian drying. *Geophysical Research Letters*, 45(6), 2815-2825. doi:10.1002/2017gl076520
- Samset, B., Myhre, G., Forster, P., Hodnebrog, Ø., Andrews, T., Faluvegi, G., et al. (2016). Fast and slow precipitation responses to individual climate forcers: A pdrmip multimodel study. *Geophysical Research Letters*, 43(6), 2782-2791. doi:10.1002/2016GL068064
 - Schmidt, G. A., Kelley, M., Nazarenko, L., Ruedy, R., Russell, G. L., Aleinov, I., et al. (2014). Configuration and assessment of the giss modele2 contributions to the cmip5 archive. *Journal of Advances in Modeling Earth Systems*, 6(1), 141-184. doi:10.1002/2013MS000265
- 430 Schmitt, R. W. (2008). Salinity and the global water cycle. *Oceanography*, 21(1), 12-19.

- Suzuki, K., & Takemura, T. (2019). Perturbations to global energy budget due to absorbing and scattering aerosols. *Journal of Geophysical Research: Atmospheres*, 124(4), 2194-2209. doi:10.1029/2018JD029808
- Takemura, T., Egashira, M., Matsuzawa, K., Ichijo, H., O'ishi, R., & Abe-Ouchi, A. (2009). A simulation of the global distribution and radiative forcing of soil dust aerosols at the last glacial maximum. *Atmospheric Chemistry & Physics*, 9(9). doi:10.5194/acp-9-3061-2009
- Takemura, T., Nozawa, T., Emori, S., Nakajima, T. Y., & Nakajima, T. (2005). Simulation of climate response to aerosol direct and indirect effects with aerosol transport-radiation model. *Journal of Geophysical Research: Atmospheres*, 110(D2). doi:10.1029/2004JD005029
- Tang, T., Shindell, D., Faluvegi, G., Myhre, G., Olivié, D., Voulgarakis, A., et al. (2019). Comparison of effective radiative forcing calculations using multiple methods, drivers, and models. *Journal of Geophysical Research: Atmospheres, 124*(8), 4382-4394. doi:10.1029/2018JD030188
 - Tang, T., Shindell, D., Samset, B. H., Boucher, O., Forster, P. M., Hodnebrog, Ø., et al. (2018). Dynamical response of mediterranean precipitation to greenhouse gases and aerosols. *Atmospheric Chemistry and Physics*, 18(11), 8439-8452. doi:10.5194/acp-18-8439-2018
- 445 Tang, T., Shindell, D., Zhang, Y., Voulgarakis, A., Lamarque, J. F., Myhre, G., et al. (2020). Response of surface shortwave cloud radiative effect to greenhouse gases and aerosols and its impact on summer maximum temperature. *Atmos. Chem. Phys.*, 20(13), 8251-8266. doi:10.5194/acp-20-8251-2020
 - Walters, D., Williams, K., Boutle, I., Bushell, A., Edwards, J., Field, P., et al. (2014). The met office unified model global atmosphere 4.0 and jules global land 4.0 configurations. *Geoscientific Model Development*, 7(1), 361-386. doi:10.5194/gmd-7-361-2014

- Watanabe, M., Suzuki, T., O'ishi, R., Komuro, Y., Watanabe, S., Emori, S., et al. (2010). Improved climate simulation by miroc5: Mean states, variability, and climate sensitivity. *Journal of Climate*, 23(23), 6312-6335. doi:10.1175/2010JCLI3679.1
 - Wilcox, E. M., Thomas, R. M., Praveen, P. S., Pistone, K., Bender, F. A. M., & Ramanathan, V. (2016). Black carbon solar absorption suppresses turbulence in the atmospheric boundary layer. *Proceedings of the National Academy of Sciences*, 113(42), 11794. doi:10.1073/pnas.1525746113
- 455 Wild, M., Ohmura, A., Gilgen, H., & Rosenfeld, D. (2004). On the consistency of trends in radiation and temperature records and implications for the global hydrological cycle. *Geophysical Research Letters*, 31(11). doi:10.1029/2003GL019188
 - Wu, J., Zha, J., Zhao, D., & Yang, Q. (2018). Changes in terrestrial near-surface wind speed and their possible causes: An overview. *Climate Dynamics*, 51(5), 2039-2078. doi:10.1007/s00382-017-3997-y
- Xu, M., Chang, C.-P., Fu, C., Qi, Y., Robock, A., Robinson, D., et al. (2006). Steady decline of east asian monsoon winds, 1969–2000:

 Evidence from direct ground measurements of wind speed. *Journal of Geophysical Research: Atmospheres, 111*(D24). doi:10.1029/2006JD007337

470

475

480

Table 1. Descriptions of the eight PDRMIP models used in this study.

Model name	Version	Resolution	Ocean setup	Aerosol setup	references
CanESM2	2010	2.8×2.8 35 levels	Coupled	Emission	Arora et al. (2011)
GISS-E2R	E2-R	2×2.5 40 levels	Coupled	Fixed concentration	Schmidt et al. (2014)
HadGEM2-ES	6.6.3	1.875×1.25 38 levels	Coupled	Emissions	Collins et al. (2011)
HadGEM3-GA	4.0	1.875×1.25 85 levels	Coupled	Fixed concentration	Bellouin et al. (2011) Walters et al. (2014)
MIROC- SPRINTARS	5.9.0	T85 40 levels	Coupled	HTAP2 emissions	Takemura et al. (2009) Takemura et al. (2005) Watanabe et al. (2010)
CESM-CAM4	1.0.3	2.5×1.9 26 levels	Slab	Fixed concentration	Neale et al. (2010) Gent et al. (2011)
CESM-CAM5	1.1.2	2.5×1.9 30 levels	Coupled	Emissions	Hurrell et al. (2013) Kay et al. (2015) Otto-Bliesner et al. (2016)
NorESM	1-M	2.5×1.9 26 levels	Coupled	Fixed concentration	Bentsen et al. (2013) Iversen et al. (2013) Kirkevåg et al. (2013)

Note: HTAP2 = Hemispheric Transport Air Pollution, Phase 2.

<u>Table 2.</u> Globally-averaged multi-model mean (MMM±1s.e.) values of changes in surface energy components and temperature per unit global TOA forcing.

Model	△Rin (W m² per W m²)	△↑LW (W m² per W m²)	ΔH (W m ² per W m ²)	ΔλΕ (W m² per W m²)	ΔBowen ratio (β per W m²)	$\triangle G$ (W m ² per W m ²)	ΔT (K per W m²)
CO_2	1.26±0.08	0.97 ± 0.05	0.50 ± 0.08	-0.42±0.10	-0.03±0.02	0.21 ± 0.02	0.18 ± 0.01
CH4	1.02±0.11	0.68 ± 0.06	0.01 ± 0.05	0.14±0.02	-0.09±0.04	0.19 ± 0.04	0.12±0.01
Solar	1.11±0.03	0.47 ± 0.04	0.19 ± 0.03	0.26 ± 0.03	-0.05±0.02	0.20 ± 0.01	0.08 ± 0.01
BC	-3.56±0.60	0.86 ± 0.36	-2.88±0.43	-1.54±0.27	-0.20±0.07	0.00 ± 0.16	0.25±0.08
SO ₄	1.54±0.14	0.54±0.09	0.32 ± 0.06	$0.44{\pm}0.07$	0.00 ± 0.02	0.24 ± 0.01	0.10±0.02

Table 3. Multi-linear regression model for each experiment.

Experiment	Regression model	Correlation coefficient (r)
CO_2	$\triangle T = 0.148 \times \triangle Rin + 0.004 \times \triangle H + 0.002 \times \triangle \lambda E$	0.89
CH ₄	\triangle T = 0.143 × \triangle Rin $-$ 0.032 × \triangle H $-$ 0.030 × \triangle λ E	0.77
Solar	$\triangle T = 0.083 \times \triangle Rin + 0.006 \times \triangle H - 0.009 \times \triangle \lambda E$	0.73
BC	\triangle T = 0.176 × \triangle Rin $-$ 0.214 × \triangle H $-$ 0.156 × \triangle λ E	0.89
SO ₄	$\triangle T = 0.072 \times \triangle Rin + 0.009 \times \triangle H - 0.020 \times \triangle \lambda E$	0.77

Table 4. Domain-averaged △T and contributions from each radiative component estimated from the linear regression model for the BC experiment (unit: K).

Region	$\triangle T$	Fitted $\triangle T$	$\triangle R_{in}$	∆Н	ΔλΕ
Global	0.08 ± 0.02	0.07	-0.19	0.19	0.07
US	0.40 ± 0.12	0.36	-0.20	0.23	0.34
Europe	0.29 ± 0.07	0.24	-0.40	0.30	0.34
E. China	0.06 ± 0.16	0.00	-2.47	1.87	0.60
India	0.19 ± 0.11	0.07	-1.50	1.38	0.20
Africa	-0.12 ± 0.06	-0.10	-2.25	1.47	0.68
S. America	0.01 ± 0.03	0.02	-0.81	0.69	0.15

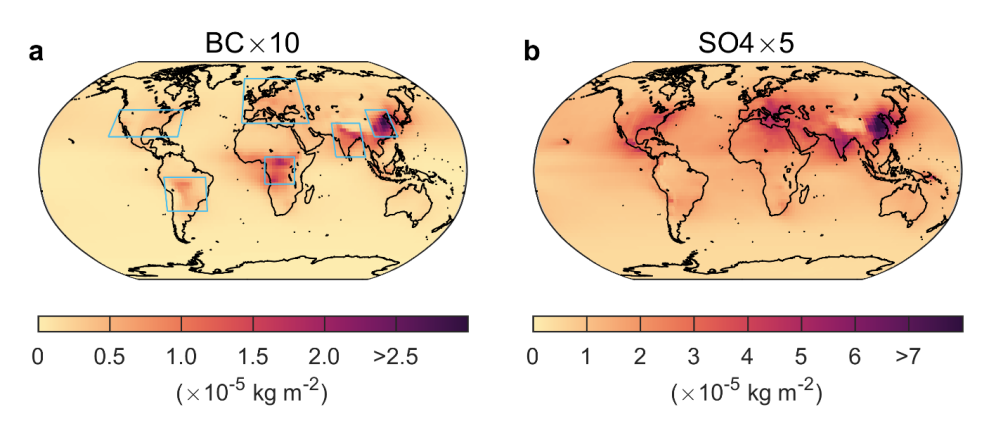


Figure 1: Aerosol loadings for the two aerosol experiments in the NorESM model.

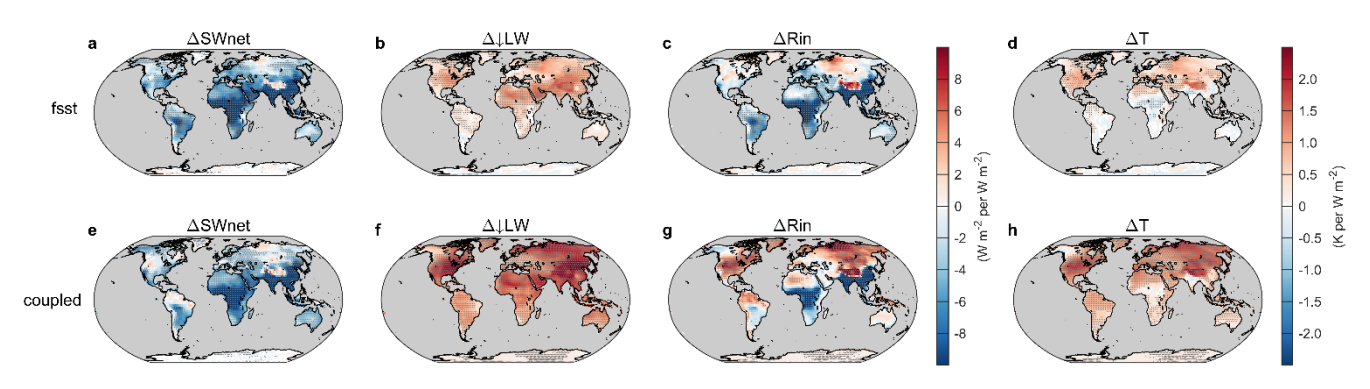


Figure 2: MMM changes of surface net SW radiation, downward LW radiation, incoming radiation (R_{in}), and surface air temperature in the fsst (a-d) and coupled simulations (e-h) for the BC experiment. All changes are normalized to changes per unit global forcing. Grey dots indicate that the MMM changes are significant at a p value of 0.05.

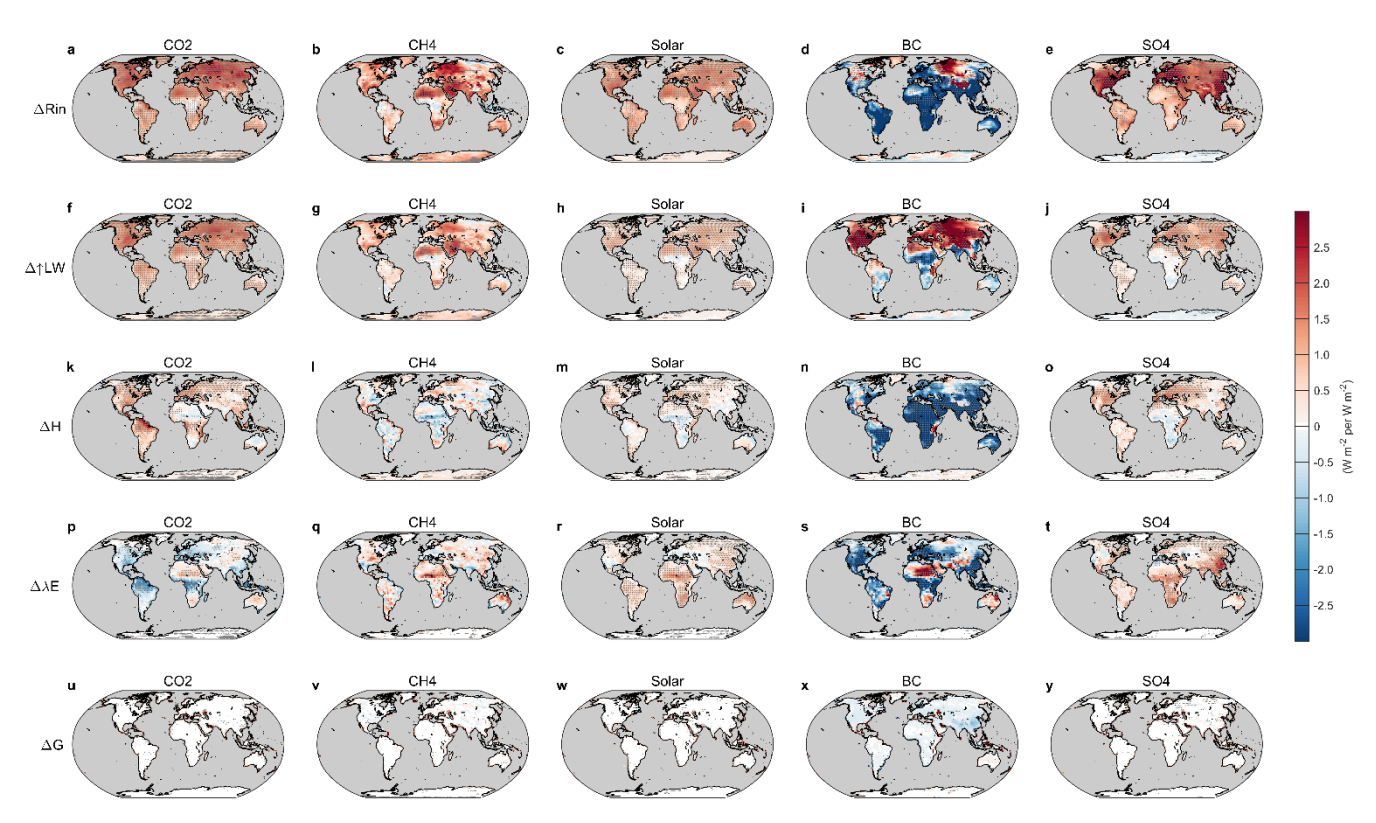


Figure 3: MMM changes of R_{in} and outgoing energy components for all five experiments in the fsst simulations. All changes are normalized to changes per unit global forcing. Grey dots indicate that the MMM changes are significant at a *p* value of 0.05.

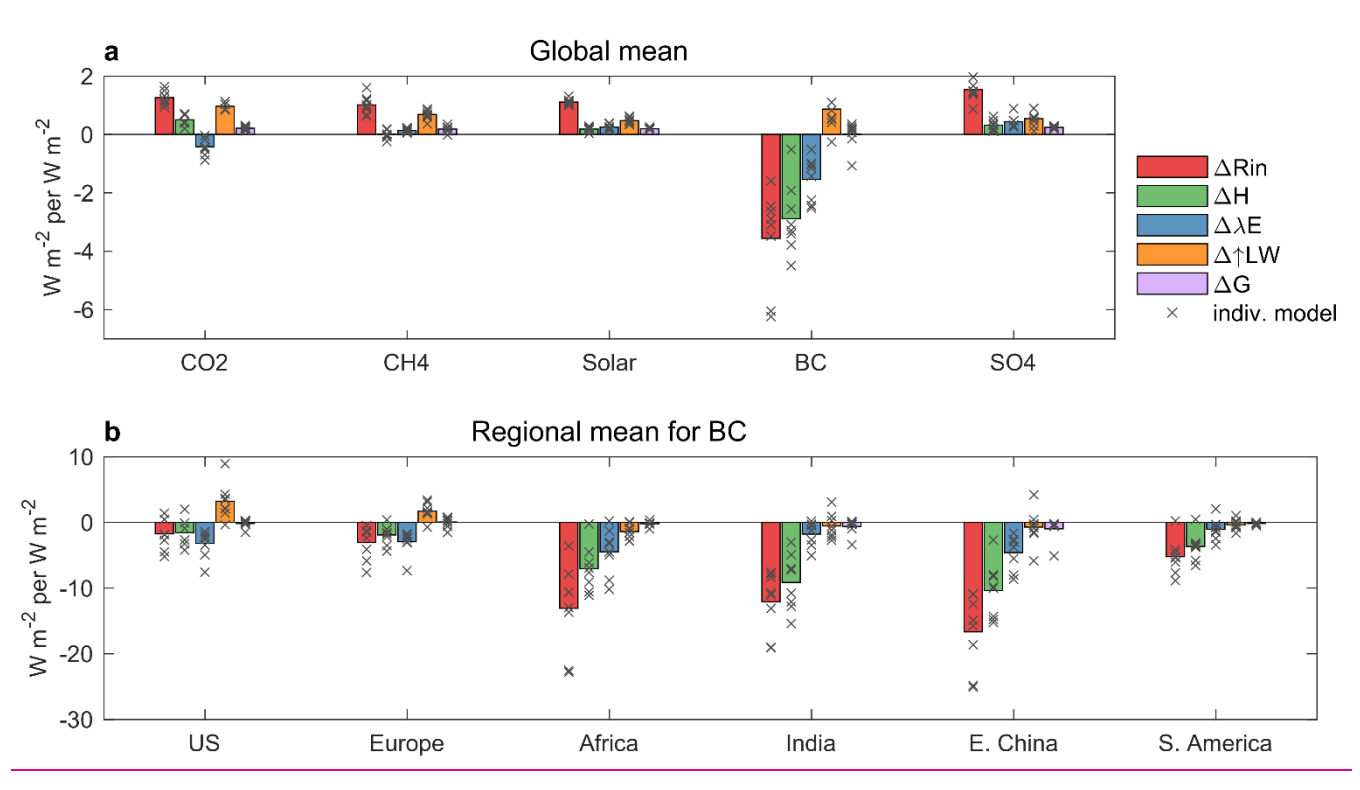


Figure 4: Domain-averaged values of R_{in} and the components of E_{out} from the fsst simulations for global mean (a) and for selected regions under BC forcing (b). \times indicates the values from individual models.

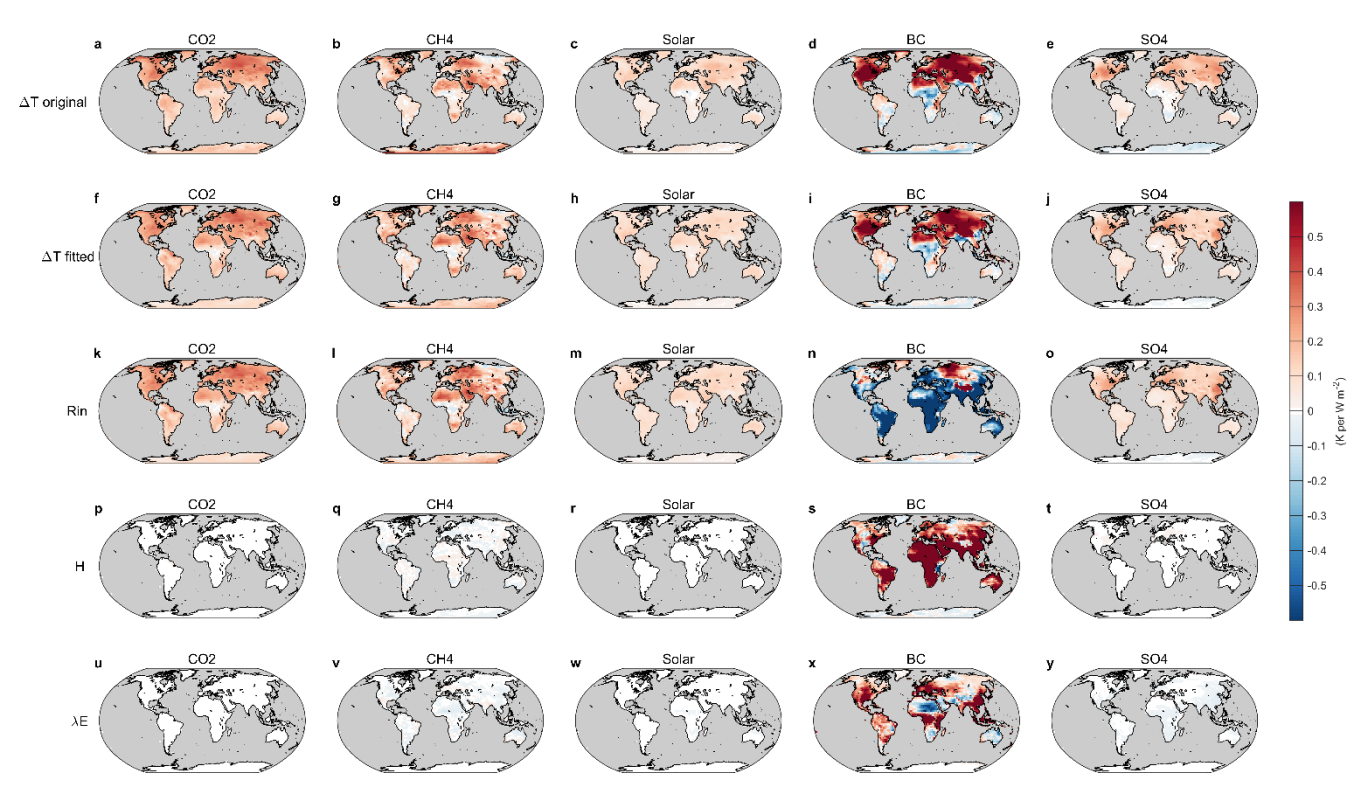


Figure 5: Air temperature change per unit forcing. Original ΔT (a-e), ΔT estimated from multi-linear regression model (f-j), and temperature change contributed by each component based on the linear regression models (k-y).

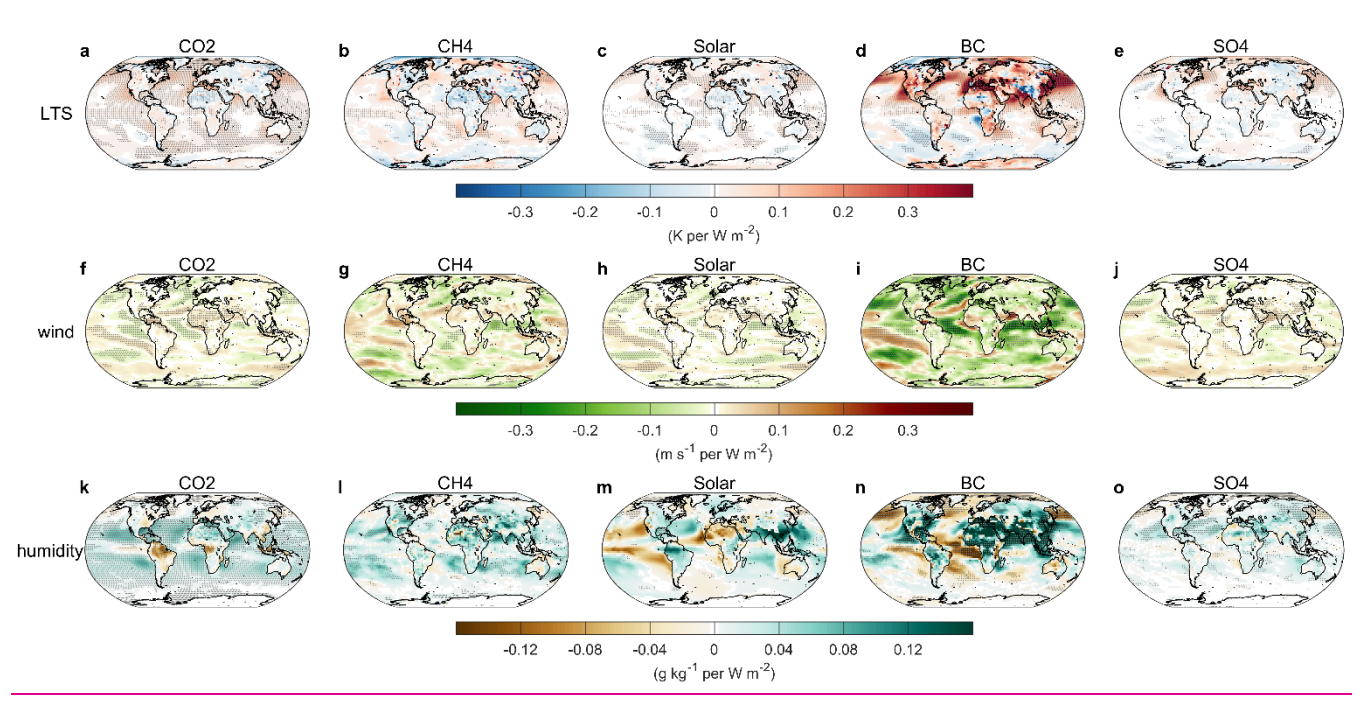


Figure 6: MMM changes for lower tropospheric stability (LTS, a-e), surface wind velocity (f-j) and humidity gradient (k-o) per unit global TOA forcing. For LTS, positive anomalies indicate a more stable atmosphere. The humidity gradient is defined as the specific humidity difference between the surface and 850 hPa. Grey dots indicate that the MMM changes are significant at a p value of 0.05.

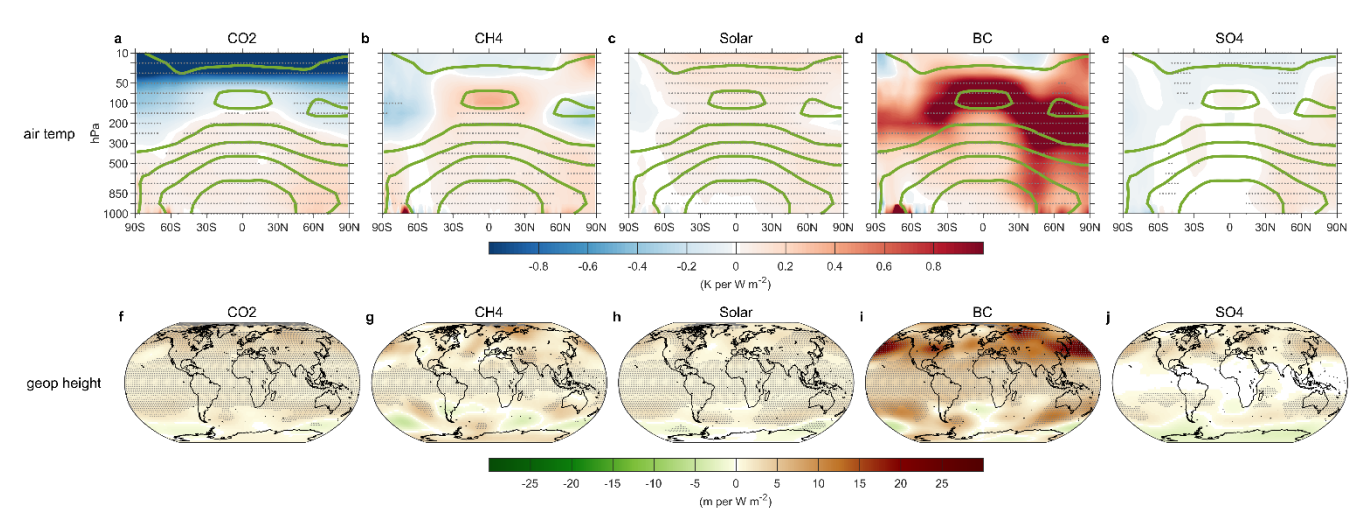


Figure 7: MMM changes for zonal atmospheric temperature (a-e) and geopotential height of 500 hPa (f-j) per unit global TOA forcing. The thick green lines in the upper row are the climatology temperature in the control simulation. Grey dots indicate that the MMM changes are significant at a p value of 0.05.

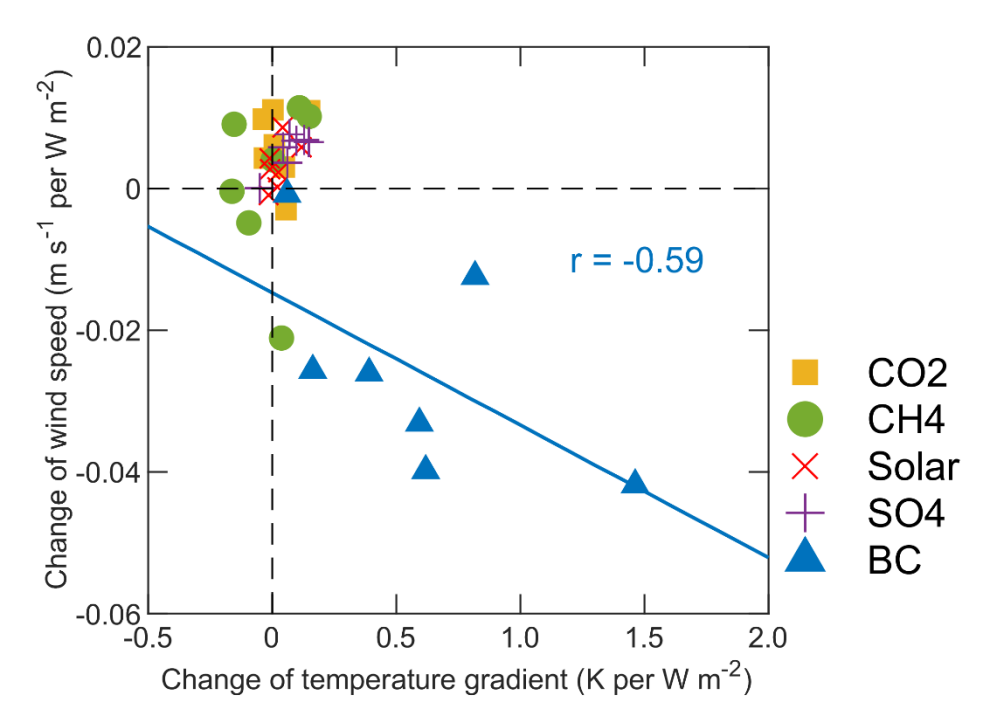


Figure 8: Changes of wind speed versus changes of temperature gradient for each individual model and simulation. The CESM1-CAM4 model is excluded due to the unavailability of surface wind data. The linear correlation r is for the BC experiment.